

pubs.acs.org/Macromolecules Article

Dynamic Worm-Gel Materials as Tunable, Regenerable Adsorbents for Water Treatment

Ali Shahrokhinia, Shayesteh Tafazoli, Sahaj Rijal, Dylan B. Shuster, Randall A. Scanga, David J. Morefield, Jaelese Garay, Raylene A. Rocheleau, Mohammad Bagheri Kashani, Ramaswamy Nagarajan, Onur G. Apul, and James F. Reuther*



Cite This: Macromolecules 2024, 57, 628-639



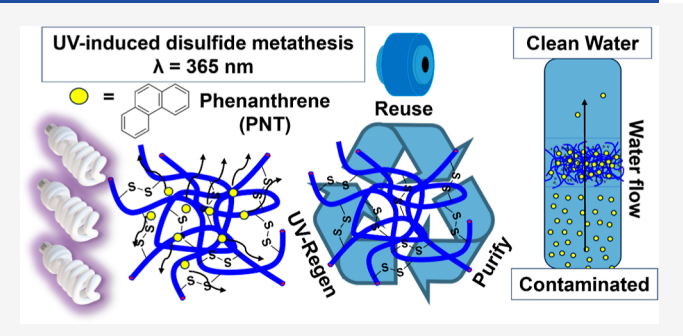
ACCESS

III Metrics & More

Article Recommendations

Supporting Information

ABSTRACT: Introducing facile regenerability into adsorbent materials can potentially increase sustainability in water treatment systems enabled by extended use. Herein, we detail our recent syntheses of dynamic nanostructured worm-gel materials and their implementation as regenerable adsorbents for water treatment. Photocontrolled atom transfer radical polymerization-induced self-assembly (PhotoATR-PISA) was employed to synthesize various polymer nanostructures, including dispersed spheres, worms, and vesicles, and nanostructured worm-gels, via the synthesis and simultaneous in situ assembly of BAB triblock copolymers. Two dynamic, disulfide-functionalized macroinitiators (SS-MI-1 and 2)



with different degree of polymerization and one nondynamic macroinitiator (CC-MI) were synthesized via polymerization of oligo (ethylene glycol methyl ether methacrylate) (OEGMA). PhotoATR-PISA was then implemented via the chain extension from SS-MI-1, 2 and CC-MI with glycidyl methacrylate (GMA) or benzyl methacrylate (BMA) forming BAB-type triblock copolymer nanoparticles in situ. The final morphology in PhotoATR-PISA was influenced not only by conventional factors such as solids content and block DP but also by unimer exchange rates yielding arrested, nanostructured worm-gels in many instances and arrested vesicle-gels in one instance. These PISA-gel materials were implemented as adsorbents for phenanthrene, a model compound registered as a priority pollutant by the US EPA, from aqueous solutions. The chemical tunability of these materials enabled enhanced, targeted removal of phenanthrene facilitated by π - π interactions, as evidenced by the increased adsorption capacities of PBMA-based PISA-gels when compared to PGMA. Furthermore, the dynamicity of disulfide worm-gels (SS-WG) enabled disulfide exchange-induced regeneration stimulated by UV light. This UV-responsive exchange was investigated for POEGMA macroinitiators as well as dissolved triblock copolymers, dispersed nanoparticles, and SS-WG materials. Finally, the regenerability of the PNT-saturated SS-WG adsorbents induced by UV irradiation (λ = 365 nm) was examined and compared with control worm-gels absent of disulfides, demonstrating enhanced recovery of adsorption capacity under mild irradiation conditions.

INTRODUCTION

In recent years, the combination of polymerization-induced self-assembly (PISA) with reversible deactivation radical polymerizations (RDRP) has opened up new possibilities for accessing a diverse range of polymeric nanoparticles (NPs) with various morphologies and sizes. $^{1-7}$ These methodologies address significant barriers to scaling up traditional self-assembly procedures, enabling the streamlined synthesis of concentrated polymeric NP dispersions with typical solids content (SC %) ranging from SC % = 25–50 wt %. Reversible addition—fragmentation chain transfer (RAFT) dispersion polymerization have been extensively investigated yielding detailed phase diagrams for many systems. 8,9 The emergence of light-mediated polymerizations has garnered considerable interest owing to distinctive advantages such as temporal and spatial control, intensity regulation, wavelength orthogonality, and mild operating conditions. $^{8,10-18}$ Of these examples,

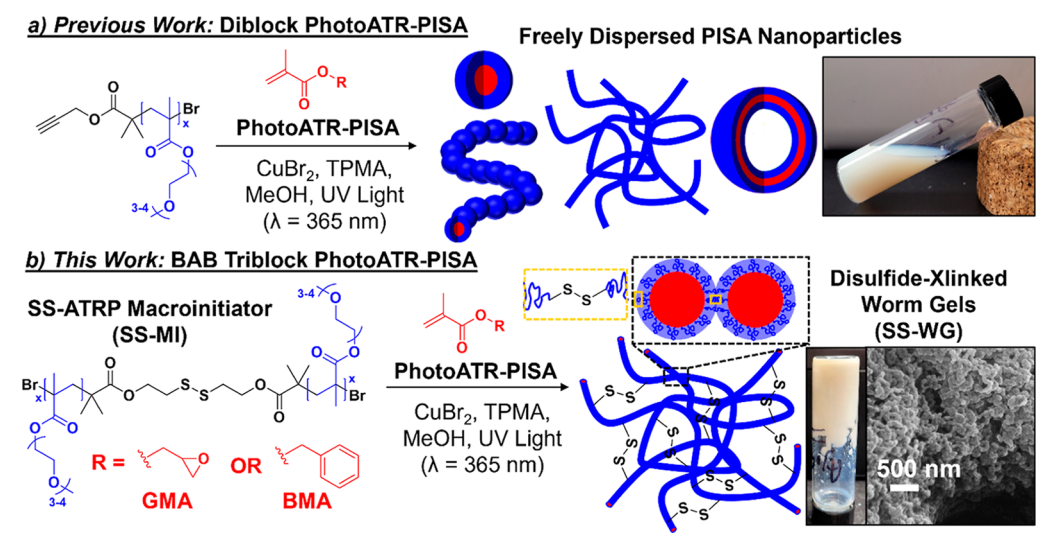
photocontrolled atom transfer radical polymerization (Photo-ATRP) methodologies provide robust capabilities of forming sequence-defined block copolymers in one-pot with high chain end fidelity. Our research group recently explored the combination of PhotoATRP and PISA (PhotoATR–PISA), mediated by UV light irradiation (λ = 365 nm). This method has enabled the preparation of diverse, core-cross-linked (CCL) morphologies ranging from spheres to vesicles at ambient temperature and provided routes to unprecedented,

Received: October 11, 2023 Revised: December 6, 2023 Accepted: December 25, 2023 Published: January 3, 2024





Scheme 1. Previous PhotoATR-PISA Synthesis of Dispersed Polymer NPs Using Monofunctional POEGMA Macroinitiators (a) and PhotoATR-PISA Synthesis of Dynamic, Disulfide-Crosslinked Worm-Gel Materials (SS-WG) Formed Via Bridged Unimer Linkages from BAB-Type Triblock Copolymers of PGMA-b-POEGMA-b-PGMA and PBMA-b-POEMGA-b-PBMA (b; Example SEM Shown)



record-high SC % = 79 wt % for dispersed polymeric tubesomes. ^{21,22}

The ability of dynamic polymeric networks to exhibit chemical and/or physical changes in response to diverse external stimuli can enable various applications. 23-28 Dynamic bonds in stimuli-responsive materials can range from supramolecular interactions (e.g., hydrogen bonding, π - π interactions, and electrostatics) to dynamic covalent bonds (DCBs). Among these DCBs, thiol/disulfide exchange reactions have garnered significant attention due to their diverse applicability and unique multiresponsivity.^{29–35} For example, disulfide bonds can show dynamic exchange in response to redox,³⁶ mechanochemical,³⁷ and light³⁸ triggers. Klumperman and colleagues utilized disulfide chemistry to fabricate a cross-linked rubber material with remarkable selfhealing capabilities.³³ Further, Wang et al. took advantage of the thiol-disulfide exchange to prepare a fast self-healing hydrogels under visible light irradiation.³⁹ These self-healing characteristics are herein applied to the regeneration of polymer-based adsorbent materials, allowing for stimuliinduced desorption of pollutants from saturated gels in response to UV light offering sustainable alternatives in water treatment.

Porous carbon-based adsorbents, such as activated carbon, are commonly employed in water treatment applications to physisorb soluble pollutants from water. 40-45 Although these adsorbents are both effective and cost-efficient, there are some drawbacks that warrant consideration. The limited synthetic tunability of activated carbon presents challenges in targeting specific contaminants in complex aqueous media. This limited tunability often leads to nonspecific adsorption of various constituents (e.g., natural organic matter) causing rapid depletion of adsorption sites. In response, the development of novel, polymer-based water treatment systems has enhanced capabilities toward targeted removal of new, emerging contaminants. 46-49 Utilizing ionic fluorogels, Leibfarth and co-workers removed a variety of per- and polyfluoroalkyl substances (PFASs) from water using gels synthesized via radical copolymerization of methacrylate-functionalized perfluoropolyethers (PFPE) and (2-dimethylaminoethyl)-methacrylate. ⁴⁶ The cationic nature of these adsorbents allowed the enhanced adsorption of PFASs through complementary electrostatic interactions. The adsorption capacity of these materials could be recovered upon washes with methanolic ammonium acetate to charge screen for PFAS adsorbates, allowing for desorption. Several studies have reported similar approaches involving washing the saturated adsorbent with salt solutions to facilitate desorption and regeneration. ^{50,51} However, the stimuli-triggered desorption of pollutants from adsorbent materials without chemical additives remains a significant challenge and has been a central focus of research among numerous research groups. ^{46,47,52,53}

In this study, dynamic, nanostructured PISA-gel materials with disulfide inter-NP cross-links were synthesized in situ and applied as regenerable adsorbents. For the first time, to the best of our knowledge, dynamic covalent exchange was employed to enable recovery of adsorption sites in response to UV-irradiation without any chemical additives. Two macroinitiators with centralized disulfide bonds (SS-MI-1, 2), and one control macroinitiator without disulfide groups (CC-MI), were implemented for PhotoATR-PISA. Upon chain extension with benzyl methacrylate (BMA) or glycidyl methacrylate (GMA), various polymer NP morphologies could be synthesized in situ with central POEGMA "A" blocks occupying the shells. Under specific conditions, these BABbased triblock copolymer NPs were assembled simultaneously with polymerization to yield arrested worm-gels with disulfide cross-links via bridged unimers (SS-WG; Scheme 1b). The resulting worm-gels exhibited efficient, rapid, and tunable PNT adsorption behavior depending on NP size, polymer microstructure, and NP morphology. The UV-induced dynamicity of the prepared nanomaterials, driven by disulfide exchange, was evaluated across different states, ranging from unimer to dispersed NPs to worm-gels. Finally, the regenerability of saturated adsorbents was assessed over multiple regeneration cycles induced only by UV light and water washes demonstrating enhanced adsorption capacity recovery for SS-WGs compared controls without disulfides.

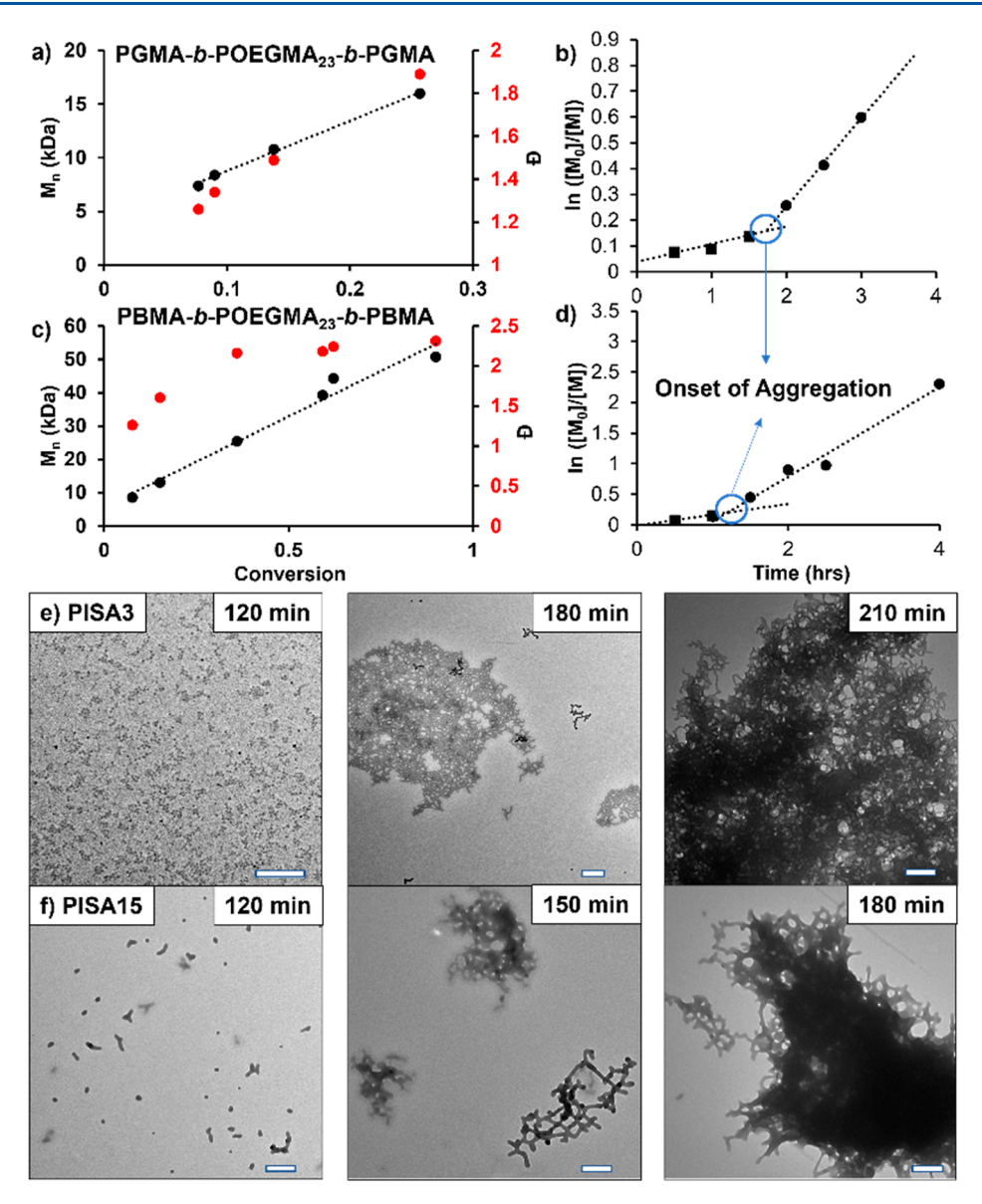


Figure 1. Plots of M_n vs monomer conversion and semilogarithmic polymerization kinetics for chain extension of PGMA (a,b) and PBMA (c,d) with SS-MI-1 at SC % = 10 wt % and DP_(core) = 300, demonstrating controlled polymerization characteristics typical of RDRP. TEM analyses (scale bars = 500 nm) were performed at different time intervals after the onset of aggregation to visualize the morphological evolution pathway that leads to arrested SS-WGs for PISA3 (e) and PISA15 (f).

■ RESULTS AND DISCUSSION

Two bifunctional ATRP initiators were synthesized via the esterification of 2-bromoisobutyryl bromide with 2-hydroxyethyl disulfide or 1,6-hexanediol to afford dynamic or nondynamic initiators, respectively, as illustrated in Figures S1 and S2. Telechelic POEGMA macroinitiators were subsequently first synthesized in 2,2,2-trifluoroethanol targeting DP_{POEGMA} = 40. The polymerization process was initiated using a commercial gel nail polish UV curing lamp ($\lambda_{max} = 365$ nm). To maintain the bromine chain-end fidelity, the macroinitiator polymerizations were halted at 51% (SS-MI-1) and 82% (SS-MI-2) monomer conversion leading to $M_p = 6.9$ and 10.2 kDa, respectively, as calculated by ¹H NMR and confirmed via GPC (Table S1). For the control macroinitiator (CC-MI), again the polymerization of OEGMA was ceased at 52% providing POEGMA-CC-MI with $M_{\rm n}$ = 6.5 kDa. After purification, the macroinitiators were thoroughly characterized using ¹H NMR and GPC, as illustrated in Figures S3-S6. The

degree of polymerization (DP) and $M_{\rm n}$ were calculated based on end group analysis, utilizing the $^1{\rm H}$ NMR chemical shifts for the methylene protons adjacent to the disulfide group at δ = 2.87 ppm in the SS-MI or well-resolved internal methylene protons at δ = 1.48 ppm in CC-MI integrated with respect to protons adjacent to pendant group POEGMA esters. The results were in good agreement with $M_{\rm n}$ values obtained from GPC and MW dispersity ranging from D = 1.31–1.37.

PhotoATR-PISA for BAB Triblock Copolymers. Subsequently, the prepared macroinitiators were chain extended with BMA or GMA during PhotoATR-PISA to form BAB-type triblock copolymer NPs. We targeted DP = 100, 200, and 300 for PGMA and PBMA blocks investigating the morphology evolution and phase diagram at SC % = 10 and 25%. The chain extension process was carried out using SS-MI-1, 2 and CC-MI, resulting in a series of BAB triblock copolymer NPs designated as PISA1-24 and Ctrl1-12, respectively. In many instances throughout this experimental matrix, PISA samples

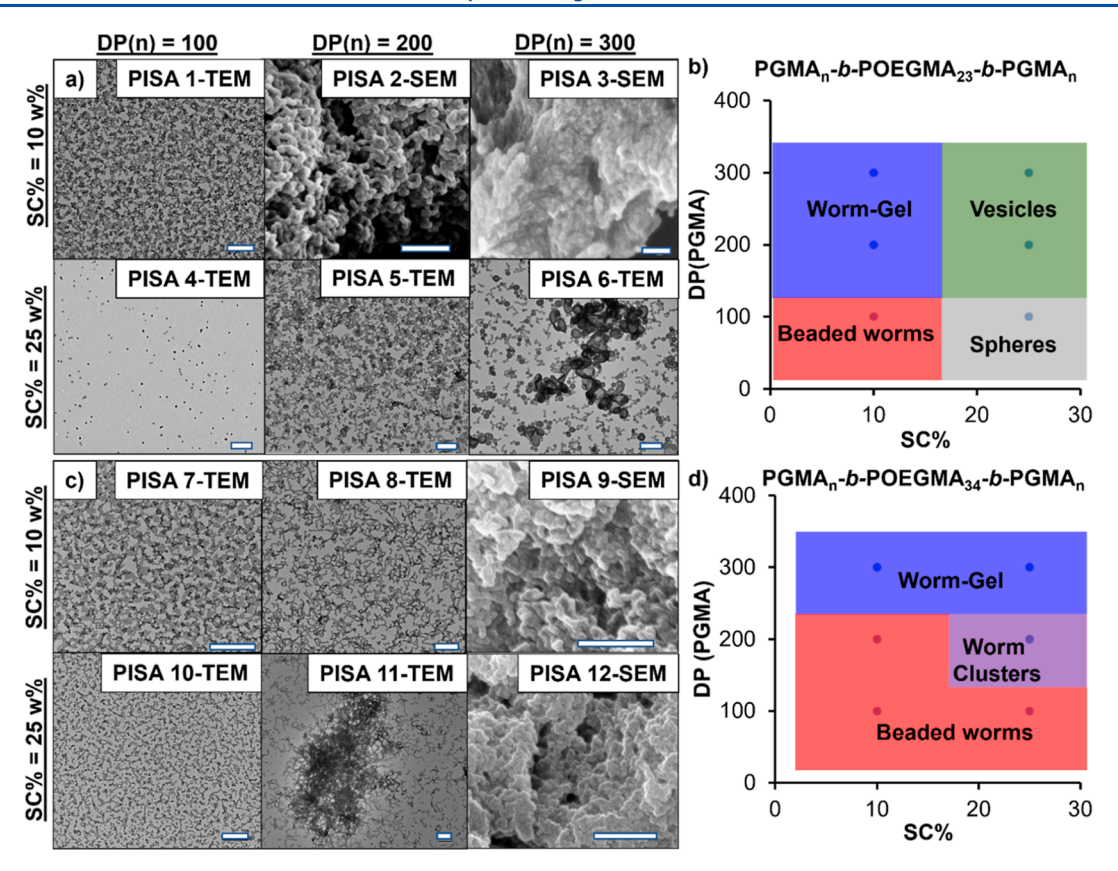


Figure 2. TEM (for NP dispersions) and SEM (for gelled reactions) images and phase diagrams for PGMA-b-POEGMA-b-POEGMA block copolymer NPs prepared via PhotoATR-PISA via chain extension with SS-MI-1 (POEGMA₂₃) (a,b) or SS-MI-2 (POEGMA₃₄) (c,d). This was investigated at SC % = 10-25 wt % and DP_{PGMA} = 100-300 with many instances resulting in arrested SS-WG materials (all scale bars = 500 nm).

resulted in gel formation leading to difficulties in GPC analyses of many samples (Figures S7, S8 and Tables S2-S4). At SC % = 10%, GPC chromatograms for PISA1-3 exhibited bimodality with peak shoulders at lower retention times (higher MW) most likely indicative of aggregation in GPC solutions. This bimodality is predominantly observed upon gel formation in PhotoATR-PISA which is difficult to disrupt for dissolution (analysis only on soluble portions of triblock copolymer with significant portions removed via syringe filtration). However, for SC % = 25% (PISA4-6), bimodality was far less prominent due to the dispersion nature of the NPs synthesized. For PISA7-12, GPC analysis was again challenging due to filtration difficulties with the only analyzed samples (PISA7, 8, and 10) representing dispersed NPs rather than gels. These, however, still exhibited bimodal GPC curves indicative of aggregation in THF. GPC analysis of PBMA-b-POEGMA-b-PBMA synthesized from SS-MI-1, except for PISA15 and 18, displayed no tangible bimodality and characterization was feasible for all samples. For BMA chain extensions with SS-MI-2, GPC analysis was only applicable for PISA19-21 with PISA20 and 21 displaying significant bimodality. Similar results were also obtained using CC-MI for both GMA and BMA chain extensions with several reactions leading to bimodal GPC peaks, demonstrating that the issue is general to these types of BAB triblock copolymers in PhotoATR-PISA (Figure S8).

To investigate the polymerization control, the kinetics of PhotoATR-PISA was monitored to confirm the living polymerization characteristics demonstrated in our previous work.²¹ As model systems, chain extensions from both SS-MI-1

(Figure 1) and CC-MI (Figure S9) were implemented with the targets of $DP_{(core)}$ = 300 and SC % = 10% for both PGMA and PBMA core-forming blocks. For GMA chain extension, early gelation caused our kinetic analysis to be only applicable for the early stage of the polymerizations (ca. <30% GMA conversion). Linear relationships between growing M_p and percent monomer conversion for both triblock copolymer systems indicate the suppression of unwanted chain-transfer side reactions. Furthermore, the linear trend for semilogarithmic kinetic plots supports the expected pseudo-firstorder kinetics typical of RDRP, albeit with one caveat (Figures 1b,d and S9a-d). Common to PISA, the polymerization rate increased substantially after 1-2 h indicating the nascent stage of micellization. As the polymerization proceeds, the hydrophobic monomers migrate into NP cores resulting in increased local monomer concentration in the vicinity of the propagating chain ends. Throughout all cases and as the PISA process progressed, the dispersity increased due to the enhanced heterogeneity at propagating centers. For two representative examples of worm-gel formation (i.e., PISA3 for PGMA and PISA15 for PBMA triblock copolymers), the morphological evolution was investigated by using transmission electron microscopy (TEM) and scanning electron microscopy (SEM) (Figure 1e,f). In each case, after the onset of aggregation at t > 12 h, transitions from small nanospheres to aggregated, entangled worm-like micelles were observed showing rapid aggregation of NPs induced by inter-NP bridging.

Phase Diagrams for BAB-Triblock PhotoATR-PISA. To investigate the scope of morphologies possible for BAB-triblock PhotoATR-PISA, various microscopy techniques,

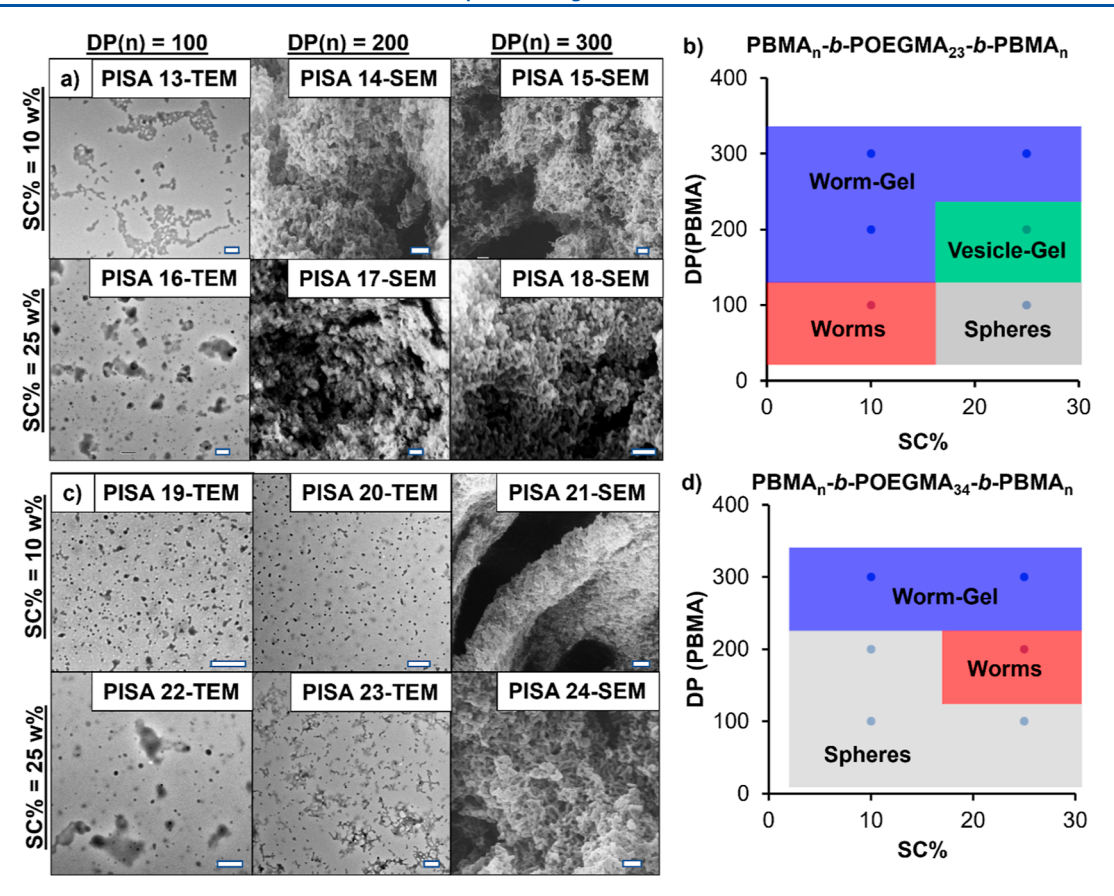


Figure 3. TEM (for NP dispersions) and SEM (for gelled reactions) images and phase diagrams for PBMA-b-POEGMA-b-PBMA block copolymer NPs prepared via PhotoATR-PISA via chain extension with SS-MI-1 (POEGMA₂₃) (a,b) or SS-MI-2 (POEGMA₃₄) (c,d). This was investigated at SC % = 10-25 wt % and DP_{PBMA} = 100-300 with many instances resulting in arrested SS-WG materials (all scale bars = 500 nm).

including TEM (for dispersions) and SEM (for gels), were employed. For PGMA chain extensions, we performed a set of 12 PhotoATR-PISA reactions (PISA1-12) ranging the SS-MI, $\mathrm{DP}_{\mathrm{PGMA}}$ = 100–300, and SC % = 10 and 25 wt % to study the phase diagram and overall accessibility of worm-gel morphologies (Figure 2). Interestingly, using SS-MI-1 (POEGMA₂₃), SS-WG morphologies were only obtained at SC % = 10 wt % with PISA4-6 forming well-dispersed NPs transitioning from small spheres to vesicles as the DP_{PGMA} increases (Figure 2a,b). Interestingly, PISA5 with target $DP_{PGMA} = 200$ yielded small vesicle structures, and PISA6 provided larger, interconnected vesicle dispersions possibly attributed to inter-NP bridging similar to SS-WGs. For PISA1-3, target DP_{PGMA} = 200 and 300 at SC % = 10 wt % yielded worm-gel morphologies whereas DP_{PGMA} = 100 led to formation of dispersed beaded worm morphologies, a common morphology observed with PGMA copolymers in PhotoATR-PISA. 21,22 For PISA7-12 synthesized with SS-MI-2 (POEGMA₃₄), the morphological evolution progressed from beaded worms and culminated in the formation of nanostructured SS-WGs for target DP_{PGMA} = 300 at both SC % (Figure 2c,d). For PISA10-12 (SC % = 25%), however, the trend diverged slightly, transitioning through entangled worm cluster dispersions at DP_{PGMA} = 200 prior to SS-WG formation at $DP_{PGMA} = 300$. When employing CC-MI for chain extension with GMA at both SC % = 10 and 25 wt %, gels were obtained when DP_{PGMA} \geq 200, but, surprisingly, Ctrl2 and 3 (SC % = 10 wt %) gels displayed little to no nanostructured worms via SEM whereas Ctrl5 and 6 yielded the previously observed worm-gels, as evidenced by

SEM (Figure S10). For target $DP_{PGMA} = 100$ (Ctrl1 and Ctrl4), small nanospheres were obtained, as evidenced by TEM.

For the PhotoATR-PISA with PBMA core-forming blocks using SS-MI-1, the morphologies transitioned from lower order morphologies when $DP_{PBMA} = 100$ (i.e., nanospheres at SC % = 10 wt % and short worms at SC % = 25 wt %) to arrested SS-WGs at target DP_{PBMA} ≥200 (Figure 3a,b). Uniquely, PISA17 $(DP_{PGMA} = 200; SC \% = 25 \text{ wt }\%)$ appeared to display different morphologies than the other worm-gels synthesized, but difficulties with surface charging during SEM imaging led to images with less than desirable resolution. To investigate this further, the morphological evolution of this gel was examined via TEM prior to gelation, revealing the formation of vesicle nanostructures that interconnect via inter-NP bridging to form arrested vesicle gels (Figure S11). For PhotoATR-PISA with SS-MI-2, the longer macroinitiator length delayed the formation of worm-gels to DP_{PBMA} = 300 for both SC % (Figure 3c,d). For SC % = 10 wt %, however, only dispersed nanospheres were observed at lower DP_{PBMA} = 100-200 (PISA19-20) whereas the formation of short, moderately tangled worm clusters was observed at target $DP_{PBMA} = 200$ and SC % = 25 wt % (PISA23). The discrepancy in phase diagram between the SS-MI-1 and SS-MI-2 systems can be attributed to the slower morphology transition rates observed when the shell-forming stabilizer blocks are longer (i.e., higher $M_{\rm p}$). 54,55 For control samples with PBMA cores synthesized using CC-MI, the trend deviates slightly (Figure S10). For instance, at SC % = 10 wt % (Ctrl7-9), dispersed worm-like

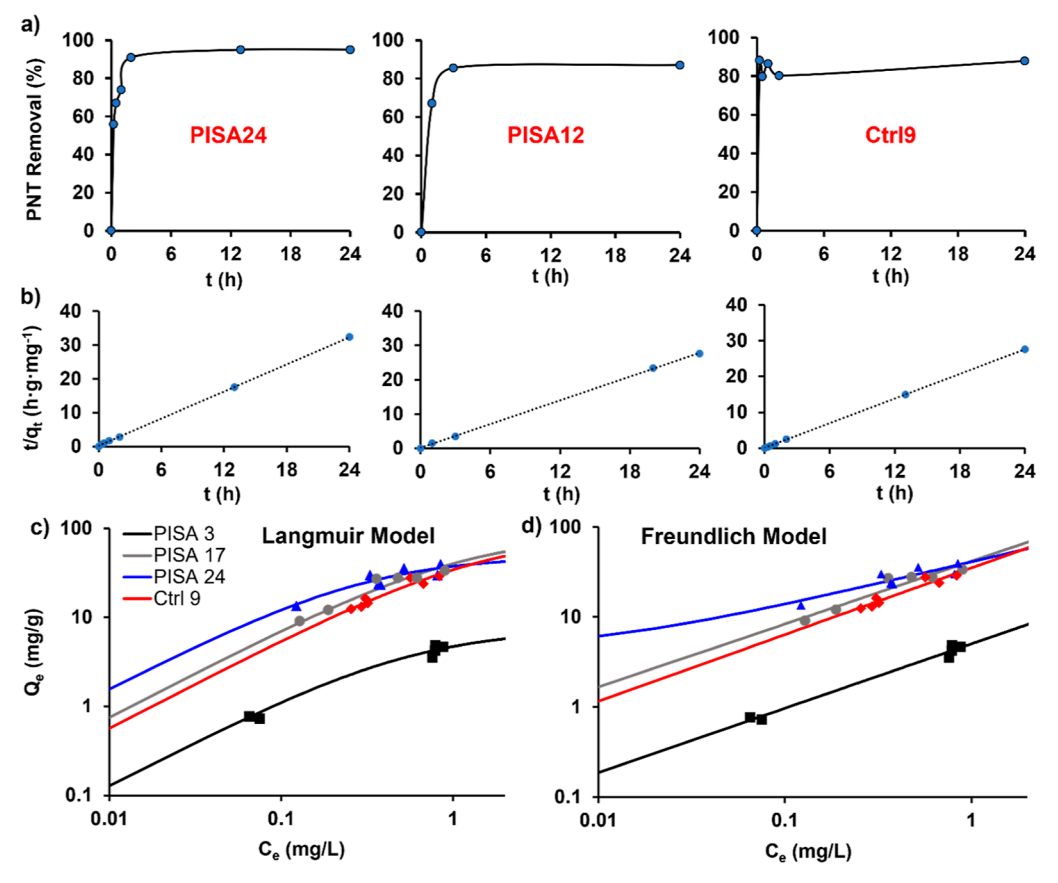


Figure 4. PNT adsorption efficiencies were monitored over the course of 24 h for PISA24, PISA12, and Ctrl9 (a) and fit to pseudo-second order kinetic models (b). PNT adsorption isotherms were constructed using PISA3, 17, 24, and Ctrl9 (adsorbent loading = 9.0-70 mg/L; c(PNT) = 1.0 mg/L; V = 1.0 L) fit to Langmuir (c) and Freundlich (d) isotherm models for quantitative characterization of adsorption capacity.

micelles were obtained when targeting $\mathrm{DP_{PBMA}} = 100-200$ which transition to arrested worm-gels at target $\mathrm{DP_{PBMA}} = 300$. Uniquely, at higher SC % = 25 wt % (Ctrl10-12), gel formation was observed at all target $\mathrm{DP_{PBMA}} = 100-300$ but SEM micrographs of each material showed no formation of worm-like nanostructures, suggesting that the presence of disulfides may help facilitate the formation of worm-gels.

In PISA for BAB triblock copolymers, there are additional factors that play critical roles in the final obtained morphology. 56-58 One essential factor is unimer exchange of hydrophobic B blocks between NPs, which drives morphology evolution. Conversely, if the exchange of B blocks is kinetically hindered, it leads to the formation of a frozen gel structures.⁵⁸ The unimer exchange rate is primarily governed by the interfacial tension between the solvophobic core and the solvent. Therefore, while an increase in the DP for the coreforming block acts as a driving force for morphology evolution, a decrease in the unimer exchange rate can shift the system toward an arrested gel state. Conversely, longer stabilizer lengths can reduce the interfacial tension between the solvophobic block and the solvent, delaying morphological evolution.⁵⁹ Furthermore, increasing SC % can accelerate morphology evolution in many PISA systems.⁶⁰ The consequences of these factors play a critical role in determining the final morphology of the system. Size analysis was conducted for all samples, considering a minimum of 50 NPs for statistical significance. It was observed that an increase in the DP led to an increase in both the size and standard deviation of the NPs (Tables S5 and S6). Specifically, wormlike micelles in worm-gels appear to thicken in diameter as the MW of triblock copolymer increases.

Removal of Phenanthrene from Aqueous Solutions Using PISA-Gels. The observed nanostructured features of worm-gel (and vesicle-gel) materials are hypothesized to facilitate potential applications in water treatment as nextgeneration adsorbents for pollutant removal. To assess the adsorptive capabilities of the prepared gels, we examined the adsorption of phenanthrene (PNT), an EPA-designated priority pollutant. PNT has found common usage as a precursor in the synthesis of dyes, plastics, and pesticides and is well-known for its toxic and carcinogenic properties. The adsorptive removal of PNT was monitored using UV-vis spectroscopy through the decrease in absorbance intensity for PNT at λ_{max} = 251 nm (Tables S2, S3 and Figure S12). The PNT-RE% of all networks ranged from 81 to 96%, with PISA15 exhibiting the highest RE % = 96% and PISA 3 exhibiting the lowest (RE % = 80%). Overall, gels formed using PBMA-based triblock copolymers provided enhanced adsorption efficiencies with 4/6 gels obtaining RE % > 90% while only 1/4 PGMA-based SS-WGs had the same level of efficiency. Subsequently, the PNT adsorption kinetics of three worm-gels (i.e., PISA24, PISA12, and Ctrl9) were investigated. After 24 h, all gels reached equilibrium with no further detectable PNT adsorption (Figure 4a; linear-fit equations are given in Figure \$13).

A pseudoequilibrium state was achieved within the first 2 h for PISA12 (RE % = 87%), PISA24 (RE % = 95%), and Ctrl9 (RE % = 87%). The kinetic data were fitted to a pseudo-

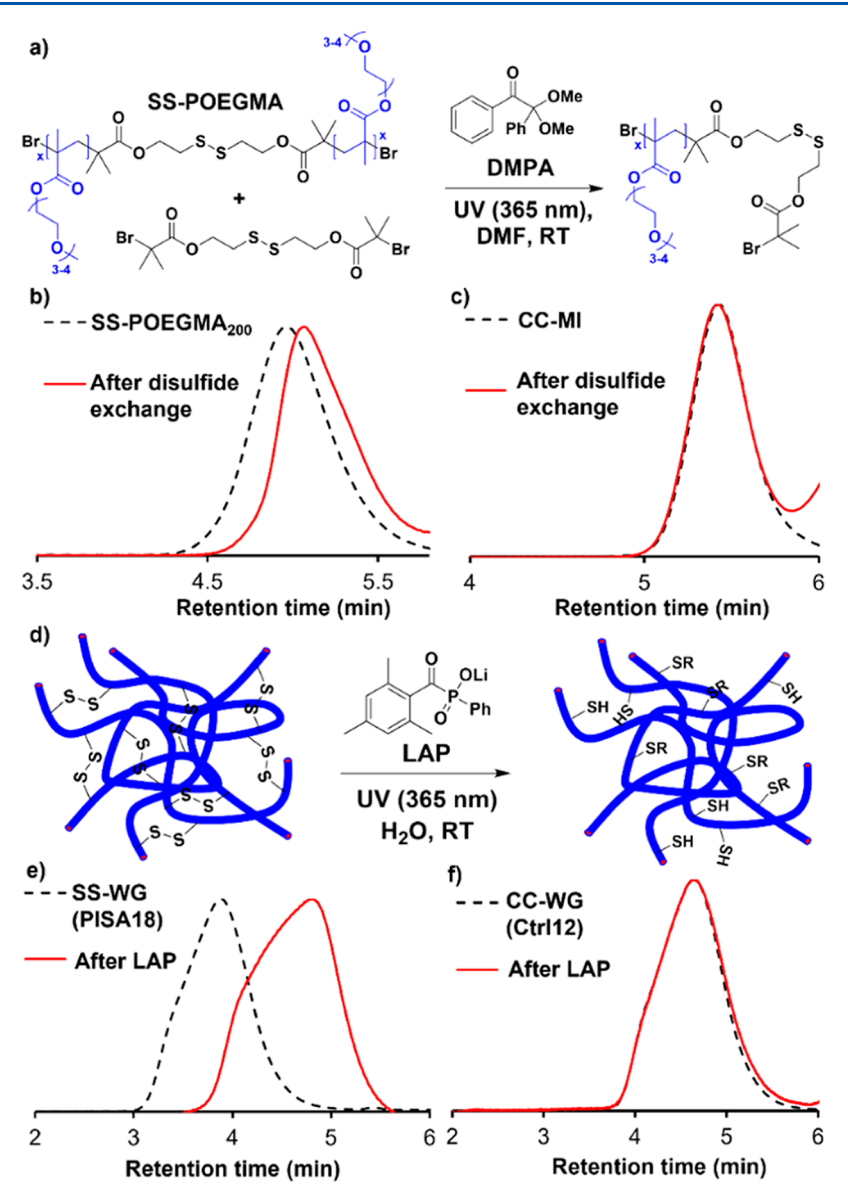


Figure 5. Dynamic cleavage and exchange in model macroinitiators with and without central disulfides using DMPA photoinitiators and disulfide ATRP initiators (a) showing clear decreases in M_n via GPC for SS-POEGMA₂₀₀ but no changes to M_n using CC-MI (b,c). Experiments were also conducted with worm-gel materials (d) PISA18 and Ctrl12 using LAP photoinitiators in water, showing similar results via GPC (e,f).

second order kinetic model (Figure 4b) and the parameters were provided in Table S7. The equilibrium adsorption capacity (q_e) values for all three gels were similar, ranging from $q_e = 0.747$ to 0.872 mg/g. However, a significant increase in the rate constant (k_2) was observed for Ctrl9 with $k_2 = 9.22$, 8.82, and 25.8 (g/mg h) for PISA12, PISA24, and Ctrl9, respectively. The faster rate of removal for Ctrl9 is attributed to the higher PNT affinity in the PBMA core-forming block and smaller diameters of the worm-like micelles (shorter PNT diffusion pathway). Subsequently, we constructed PNT adsorption isotherms for various worm-gels (PISA3, PISA24, and Ctrl9) and PISA17 (vesicle-gel) to determine the maximum adsorption capacity of various samples.

When assessing the initial isotherm data clusters, the first apparent observation is related to the dramatically lower adsorption capabilities for PISA3 compared to PISA24, PISA17, and Ctrl9. This can also be attributed to the weaker intermolecular interactions for PGMA-based SS-WGs (i.e., PISA3) due to the absence of intermolecular interactions. The

obtained data were then fitted to both the Freundlich and Langmuir adsorption models to obtain quantitative information on overall adsorption behavior. Overall, both models fit well to the data with the Langmuir model providing slightly higher R² values demonstrating better model fit. This model provided values of K_L = 3.29 and 1.76 L/mg and estimated maximum PNT adsorption capacity $Q_m = 48.7$ and 7.36 mg/g for PISA24 and PISA3 SS-WGs, respectively (Figure 4c,d and Table S8). Subsequently, analogous isotherm experiments were conducted for Ctrl9 and PISA17 to examine the effect of gel morphology and worm-like micelle size on adsorption of PNT. The Langmuir model yielded maximum PNT adsorption capacity of Q_{max} = 84.9 and 85.4 mg/g, along with K_L = 0.672 and 0.885 L/mg for Ctrl9 and PISA17, respectively. The alteration of gel morphology for PISA17 also enabled enhanced adsorption capacity reaching the largest Q_{max} value calculated for all PISA-gels, demonstrating another area of tunability for adsorbent design.

Applying the Freundlich model to the isotherm data yielded Freundlich constants of $K_F = 35.0$, 41.7, 40.8, and 5.03 (mg/ $g)(L/mg)^{1/n}$ for Ctrl9, PISA17, PISA24, and PISA3, respectively. PISA24, Ctrl9, and PISA17 (with PBMA cores) exhibited substantially higher affinity for PNT as evidenced by its higher $K_{\rm F}$. This phenomenon can be attributed to the $\pi-\pi$ interaction between PBMA cores in PISA-gels and PNT, making it more favorable for PNT removal. These findings highlight the tunability of these adsorbents, allowing targeted contaminant removal and optimization of adsorption capacity through tailored incorporation of diverse monomer functionalities into NP cores or shells. The calculated Freundlich constants were compared to conventional adsorbents such as GAC as previously reported.⁶¹ The observed adsorption capacities for PISA-gel materials were significantly lower than those for GAC $(K_F = 153.9 \text{ (mg/g)}(L/\text{mg})^{1/n} \text{ for GAC})$ showing many potential areas for improvement, which will be examined in future work. Additionally, the observed slope for PISA24 was smaller than PISA17 and Ctrl9 due to the lower calculated n value with n = 1.35, 1.43, 2.06, and 1.40, for Ctrl9, PISA17, PISA24, and PISA3. This suggests that the adsorption sites within the PISA24 worm-gel matrix are more heterogeneous than PISA17 and Ctrl9. This can be attributed to the smaller, more uniform diameters of worm-like micelles in Ctrl9 with $d(avg) = 63.5 \pm 13.8$ nm compared to PISA24 with $d(\text{avg}) = 139 \pm 35 \text{ nm}$. The lower worm diameter is expected to facilitate enhanced PNT network diffusion and the lower uniformity for nanostructure size can create PNT adsorption sites with different binding efficiencies. Due to the deformation of the worm-gels under cryogenic conditions, it was not feasible to quantitatively assess surface area and pore-size distributions using Brunauer-Emmett-Teller surface area analysis.

Dynamic Cleavage and Exchange in Disulfide NP Bridges. In recent years, polymeric materials that exhibit physical/chemical alterations in response to an external stimulus such as light have attracted significant attention.⁶² In this vein, we sought to explore UV-responsiveness of various model polymers, controls, and SS-WG materials. Disulfides are well-known to undergo photoinduced metathesis in response to UV-light and radical-induced cleavage using Type I photoinitiators. 63 First, we examined this cleavage and exchange at the unimer state for model polymers. For this, POEGMA₂₀₀ was prepared using the disulfide ATRP initiator (SS-POEGMA₂₀₀). Initial experiments utilized UV-light alone without photoinitiator, but no disulfide cleavage/exchange could be quantified via GPC or NMR despite the anticipated disulfide exchange under irradiative conditions. Comparatively, SS-POEGMA₂₀₀ and CC-MI (1.0 equiv) were mixed in DMF with equivalent molar amounts of disulfide ATRP initiators (for exchange) and different molar ratios (0.0010-2.0 equiv) of dimethoxy-2-phenylacetophenone (DMPA) photoinitiators. After 24 h of reaction under UV irradiation, the disulfide exchange was monitored by GPC (Figures 5a, S14, Tables S9 and 10) and ¹H NMR (Figure S15). For these reactions, the retention time for SS-POEGMA₂₀₀ ($M_n = 23.4 \text{ kDa}$) increased, indicating a decrease in MW consistent with cleavage and exchange of central disulfides within the polymer backbone. Surprisingly, DMPA molar ratio did not have significant effects on the extent of the reaction with consistent $M_{\rm n}$ = 17.4–18.5 kDa postexchange and complete exchange observed with as little as 0.25 equiv of DMPA (Figure 5b). These values deviate slightly from the expected halving of M_n postexchange, but the unimodal nature of the transition suggests that the exchange did indeed take place.

¹H NMR analysis comparing the starting material and final product provided additional experimental evidence for the proposed exchange reaction (Figure S15). Specifically, the signal at δ = 4.45 ppm, corresponding to the methylene proton adjacent to the SS-initiator ester group (labeled as 2), is observed to split into multiple environments (labeled as 2' and shifted to $\delta = 4.3-4.5$ ppm). Furthermore, the methylene proton adjacent to the disulfide group at δ = 2.98 ppm (labeled as 1) shifts upfield and broadens signifying attachment of the small molecule initiator to the terminal ends of SS-POEGMA₂₀₀ (labeled as 1' at $\delta = 2.7-3.0$ ppm). Integration of peak 2 relative to 2' provides information on the extent of disulfide exchange, which was calculated to 70% conversion. For CC-MI under the same exchange conditions, superposition of the GPC peaks before and after treatment provides supportive evidence that observed changes in SS-POEGMA₂₀₀ are indeed consequence of disulfide exchange, which is absent for CC-MI (Figure 5c, Table S10 and Figure S14).

Radical-induced disulfide exchange was also investigated for PISA1 ([PISA1]/[S-S Int]/[DMPA] = 1:1:0.1) both in good solvent (DMF) for both blocks (unimer state) and MeOH (assembled state), and the results were evaluated by both GPC and ¹H NMR (Figures S16—S18 and Table S11). In both cases (MeOH and DMF), there was a shift toward a lower retention time with larger shifts observed in DMF. This is hypothesized to be attributed to the enhanced accessibility of the disulfide bond in the unimer state. ¹H NMR spectra of the starting material and the final product in DMF and MeOH (after reacting with 2.0 equiv of DMPA) revealed similar alterations in chemicals shifts as described previously. The same method was used to calculate the disulfide exchange efficiency, demonstrating the 71 and 63% conversion, in DMF and MeOH, respectively (Figures S16 and S17).

To investigate the dynamic disulfide exchange in the wormgel state and in water, we selected a common water-soluble type I photoinitiator, lithium acylphosphinate (LAP). For comparison, one disulfide-functional SS-WG (PISA18) and one nondynamic worm-gel (Ctrl12) were selected and analyzed via TEM, GPC, and 31P NMR before and after photoinitiation. After UV irradiation in the presence of LAP (80 mM), GPC analysis was performed for PISA18 showing clear shifts to higher retention times compared to the original gel, indicative of disulfide scission (Figure 5e). In contrast, applying the same procedure to Ctrl12 yielded no significant change to GPC peaks before and after irradiation (Figure 5f and Table S12). 31P NMR analysis revealed the presence of three distinct peaks at δ = 7.8, 8.9, and 32.1 ppm, indicating the existence of three phosphorus-containing species postreaction (Figure S19). The peak at $\delta = 8.9$ ppm corresponds to the unreacted LAP photoinitiator, while the peak at $\delta = 7.8$ ppm is associated with the hypophosphonate, which results from the combination of two phosphine radicals. Additionally, the peak at δ = 32.1 ppm is consistent with the phosphonothioic acid ester via radical combination of thiyl and phosphine radicals.⁶³ SEM images of the gel before and after LAP solution treatment were compared, demonstrating the integrity and endurance of the worm-gels during UV treatment (Figure S20). Differential scanning calorimetry (DSC) was performed on both PISA24 and Ctrl9 worm-gel samples to gain insights into their chain mobility and its role in dynamicity (Figure S21). The DSC analysis revealed that

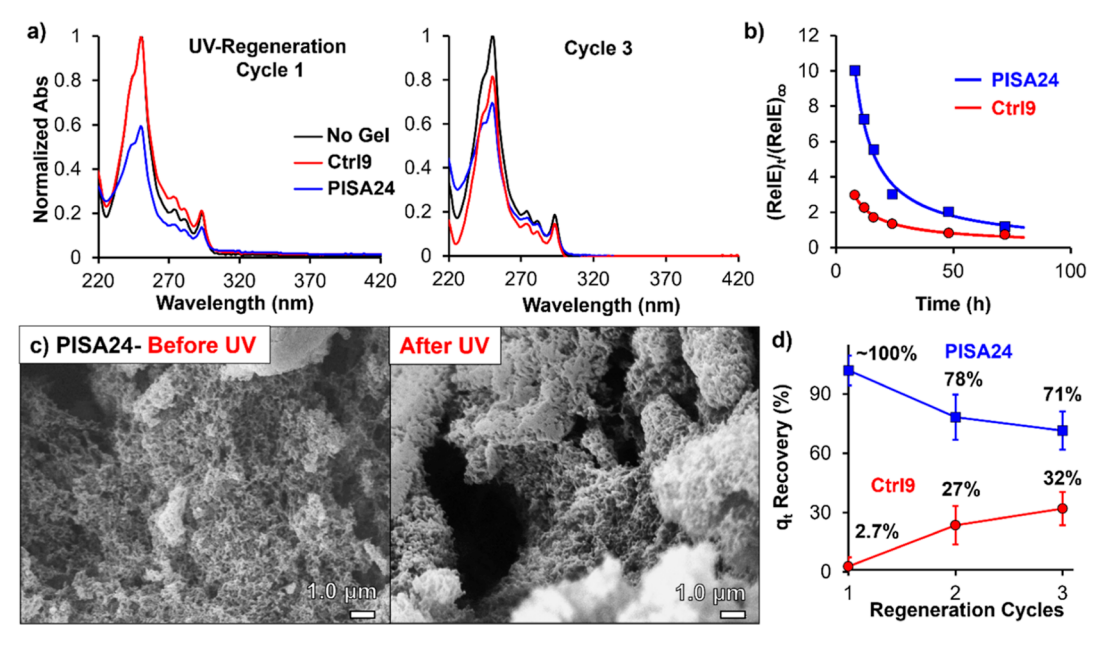


Figure 6. Adsorbent regenerability for PISA24 and Ctrl9 worm-gels via UV irradiation during water flushes postsaturation as characterized via subsequent adsorption experiments performed after regeneration (a) adsorbent loading = 18.0 mg; [PNT] = 1.00 mg/L in 25 mL water; t = 45 min. The kinetics of PNT release was measured using a power-law model inspired by the Korsmeyer-Peppas model for drug delivery (b). SEM images for PISA24 before and after three cycles of UV irradiation show nanostructural stability during regeneration procedures (c). The overall q_t recovery for both PISA24 and Ctrl9 were calculated based on obtained kinetic data for three UV-regeneration cycles (d).

PISA24 and Ctrl9 exhibited glass transition temperatures $T_{\rm g}$ = 62 and 57 °C, respectively. These results indicate that both networks were in a glassy state at ambient temperature (operational conditions).

UV-Induced Regeneration of SS-WG Adsorbents. Motivated by the initial findings, we now sought to explore the UV-regenerative potential of these polymeric worm-gel adsorbents for multiple cycles of PNT removal. We hypothesized that the exchangeability of disulfide-cross-linked systems could be applied to induce regeneration in adsorbent materials much in the same way this approach has been heavily implemented for network self-healing. 64,65 For this, we posit the use of UV-light to induce disulfide exchange without any chemical additives to allow for the stimuli-induced desorption of PNT pollutants from saturated gels. To investigate this, we subjected 18.0 mg of the PNT-saturated PISA24 and Ctrl9 worm-gels (both prepared using PhotoATR-PISA with DP_{PBMA} = 300) to UV exposure (λ_{max} = 365 nm) for 72 h in 25.0 mL water without photoinitiator and the release of PNT was monitored. The release kinetics of PNT were determined by using a power-law model. Initially, release efficiency (RelE) was computed for a more precise comparison, utilizing the provided calibration curve for PNT. Drawing inspiration from the Korsmeyer–Peppas model, 66,67 data points were fit to eqs S5 and S6. Subsequently, the K_{KP} and n values were derived (refer to Table S14), and the resulting functions were visualized in Figure 6b. Specifically, the values obtained were $K_{\rm KP} = 73.71$ and 12.77 (hⁿ) for PISA24 and Ctrl9, respectively, demonstrating the faster rate of release observed for the dynamic PISA24 SS-WG which is hypothesized to relate to enhanced diffusion through the SS-WG material under exchange conditions. Furthermore, values of n = 0.9505 and 0.7039 were calculated for PISA24 and Ctrl9, respectively, indicating that the deceleration of release is comparable for each system. Consequently, the overall release efficiency for PISA24 was found to be higher compared to Ctrl9, attributed

to the more dynamic characteristics of PISA24 due to disulfide exchange, stimulated by UV irradiation. When considering the Korsmeyer–Peppas model with 0.5 < n < 1, an anomalous transport mechanism governed by the relaxation of the polymeric chains and non-Fickian diffusion can be assigned for the given system relating to PNT release. 68,69

The UV-absorbance intensity of the released PNT was monitored every 2 h using UV—vis spectroscopy. Subsequently, fresh water was introduced into the system, and irradiation was continued until no appreciable PNT release was observed. After UV-regeneration, PNT adsorption tests were again conducted using the recovered gels using 1.0 ppm of PNT solutions. Subsequently, additional regeneration cycles and adsorption tests were conducted three times consecutively for both PISA24 and Ctrl9 (Figure 6).

After the first UV-regeneration cycle, the saturated Ctrl9 worm-gel exhibited negligible PNT adsorption (RE % = 1.6%, $q_t = 0.022 \text{ mg/g}$) while PISA24 showed significantly higher PNT removal at 46% ($q_t = 0.638 \text{ mg/g}$) within the same time frame (ca. 45 min adsorption) which represents a ~102% recovery of adsorption capacity (q_t) under the same loading. Conversely, performing the same adsorption experiment with saturated PISA24 worm-gels prior to UV treatment yielded negligible PNT adsorption (Figure S22) exemplifying the role of disulfide exchange in regeneration. After repeating the regeneration and subsequent PNT adsorption for two additional cycles (Figure 6), PISA 24 maintained PNT removal at RE % = 35% ($q_t = 0.486 \text{ mg/g}$; 78% q_t recovery) and 32% ($q_t = 0.444 \text{ mg/g}$; 71% q_t recovery) for the second and third regeneration cycle, respectively, while Ctrl9 displayed RE % = 14% (q_t = 0.194 mg/g; 23% q_t recovery) and 19% (q_t = 0.264 mg/g; 32% q_t recovery). The diminishing Q_t recovery with each regeneration cycle can be explained by the nonquantitative release of PNT during disulfide exchange. Since all PNT is not being released in each cycle, only some adsorption sites are opened during regeneration, leading to

decreased efficiencies with each subsequent cycle. PISA24 demonstrated a superior capability for q_t recovery, ranging from 100% in the first cycle to 71% in the third cycle, compared to Ctrl9, which exhibited a q_t recovery of 2.7% in the first cycle and 32% in the third cycle. These results are exacerbated when considering the higher maximum adsorption capacity (Q_{max}) of Ctrl9 compared to PISA24. Despite this, the removal efficiencies for PISA24 all surpassed those for Ctrl9 after each regeneration cycle further supporting the proposed hypothesis of exchange-induced regeneration. SEM analysis was performed on PISA24 before and after UV exposure (Figure 6b), confirming the preservation of nanostructure integrity postregeneration. The release of PNT from PISA-gel matrices is hypothesized to be facilitated by increases in molecular diffusion under disulfide exchange conditions, leading to preferential desorption under UV-irradiation. This hypothesis will be rigorously tested in follow-up work. Overall, these findings offer novel insights into sustainable adsorbent design, providing unique routes to regenerable water treatment materials facilitated by dynamic covalent exchange. Current work is focused on increasing disulfide cross-link density to intensify regenerability in polymer-based adsorbents while also introducing functionalities to target pollutants of emerging concern.

CONCLUSIONS

In this study, PhotoATR-PISA was employed to fabricate a variety of nanostructures, including spheres, worms, vesicles, and worm-gels, upon BAB triblock copolymer synthesis. Disulfide centralized POEGMA macroinitiators of different lengths (DP = 23 and 34 for SS-MI-1 and 2, respectively) were synthesized along with one control macroinitiator absent of disulfides (CC-MI). These were then chain-extended with either GMA or BMA at different solid contents (SC% = 10 and 25%) and $DP_{PBMA/PGMA}$ = 100, 200, and 300. The study revealed that, apart from the well-known factors such core DP, stabilizer DP, and SC %, unimer exchange of hydrophobic PBMA and PGMA blocks is crucial to maintain morphological evolution. When unimer exchange becomes sufficiently slow, arrested PISA-gels resulted with retained worm-like micelle morphologies (i.e., worm-gels) in the majority of gelated samples as well as one example of arrested vesicle-gels. Next, these worm-gel and vesicle-gel materials were applied as adsorbents for water treatment investigating the removal of PNT, an EPA-designated priority contaminant, from aqueous solutions. These PISA-gels exhibited a rapid uptake of PNT reaching equilibrium within 2 h in most cases. The adsorption characteristics and capacities were found to heavily depend on various factors such as NP size, morphology, and chemical composition with the most effective PNT removal observed for PBMA-based gels, smaller NP sizes, and vesicle-gel morphologies. The dynamic disulfide bridges were found to be UVactive with and without photoinitiators, with clear evidence of UV-induced disulfide exchange as confirmed via ¹H NMR and GPC in the unimer, assembled (dispersion), and gel states. Finally, this UV-induced dynamicity was applied for the recovery of the adsorption capacity in PNT saturated wormgels over multiple regeneration cycles. In this study, the disulfide-functional PISA24 worm-gels showed superior capabilities in adsorption capacity (q_t) recovery (100–71% regeneration) over all three cycles when compared to one nondynamic, control worm-gel Ctrl9 (1-32% regeneration). This work introduced a brand-new design paradigm in the

fabrication of next-generation, regenerable adsorbents, taking advantage of dynamic covalent exchange to facilitate sustainable water treatment.

ASSOCIATED CONTENT

Supporting Information

The Supporting Information is available free of charge at https://pubs.acs.org/doi/10.1021/acs.macromol.3c02090.

Additional materials and experimental details, procedures, characterization, and data supporting the claims of the manuscript (PDF)

AUTHOR INFORMATION

Corresponding Author

James F. Reuther — Department of Chemistry, University of Massachusetts Lowell, Lowell, Massachusetts 01854, United States; orcid.org/0000-0001-5611-0290; Email: james reuther@uml.edu

Authors

- Ali Shahrokhinia Department of Chemistry, University of Massachusetts Lowell, Lowell, Massachusetts 01854, United States
- Shayesteh Tafazoli Department of Chemistry, University of Massachusetts Lowell, Lowell, Massachusetts 01854, United States
- Sahaj Rijal Department of Chemistry, University of Massachusetts Lowell, Lowell, Massachusetts 01854, United States
- Dylan B. Shuster Department of Chemistry, University of Massachusetts Lowell, Lowell, Massachusetts 01854, United States
- Randall A. Scanga Department of Chemistry, University of Massachusetts Lowell, Lowell, Massachusetts 01854, United States
- David J. Morefield Department of Chemistry, Johns Hopkins University, Baltimore, Maryland 21218, United States
- Jaelese Garay Department of Chemistry, University of Massachusetts Lowell, Lowell, Massachusetts 01854, United States
- Raylene A. Rocheleau Department of Chemistry, University of Massachusetts Lowell, Lowell, Massachusetts 01854, United States
- Mohammad Bagheri Kashani Department of Plastics Engineering, University of Massachusetts Lowell, Lowell, Massachusetts 01854, United States
- Ramaswamy Nagarajan Department of Plastics Engineering, University of Massachusetts Lowell, Lowell, Massachusetts 01854, United States; orcid.org/0000-0003-2355-9547
- Onur G. Apul Department of Civil and Environmental Engineering, University of Maine, Orono, Maine 04469, United States; orcid.org/0000-0002-2964-8279

Complete contact information is available at: https://pubs.acs.org/10.1021/acs.macromol.3c02090

Notes

The authors declare no competing financial interest.

ACKNOWLEDGMENTS

This material is based upon work supported by the National Science Foundation under grant 2125727, and any opinions,

findings, and conclusions, or recommendations expressed in this material are those of the author(s) and do not necessarily reflect the views of the National Science Foundation. We would like to thank the UML Core Research Facilities (CRF) staff for their help in data acquisition, most notably Wendy Gavin for her help in NMR analysis and Earl Ada for his help in TEM analysis.

REFERENCES

- (1) Wan, J.; Fan, B.; Thang, S. H. RAFT-mediated polymerization-induced self-assembly (RAFT-PISA): current status and future directions. *Chem. Sci.* **2022**, *13* (15), 4192–4224.
- (2) Niu, B.; Chen, Y.; Zhang, L.; Tan, J. Organic-inorganic hybrid nanomaterials prepared via polymerization-induced self-assembly: recent developments and future opportunities. *Polym. Chem.* **2022**, *13* (18), 2554–2569.
- (3) Li, C.; Zhao, W.; He, J.; Zhang, Y.; Zhang, W. Single-Step Expeditious Synthesis of Diblock Copolymers with Different Morphologies by Lewis Pair Polymerization-Induced Self-Assembly. *Angew. Chem., Int. Ed. Engl.* **2022**, *61* (24), No. e202202448.
- (4) Lages, M.; Gil, N.; Galanopoulo, P.; Mougin, J.; Lefay, C.; Guillaneuf, Y.; Lansalot, M.; D'Agosto, F.; Nicolas, J. Degradable Vinyl Copolymer Nanoparticles/Latexes by Aqueous Nitroxide-Mediated Polymerization-Induced Self-Assembly. *Macromolecules* 2022, 55 (21), 9790–9801.
- (5) Fan, B.; Wan, J.; Zhai, J.; Teo, N. K. S.; Huynh, A.; Thang, S. H. Photoluminescent polymer cubosomes prepared by RAFT-mediated polymerization-induced self-assembly. *Polym. Chem.* **2022**, *13* (29), 4333–4342.
- (6) Ikkene, D.; Arteni, A. A.; Boulogne, C.; Six, J.-L.; Ferji, K. Multicompartment Vesicles: A Key Intermediate Structure in Polymerization-Induced Self-Assembly of Graft Copolymers. *Macromolecules* **2022**, *55* (11), 4268–4275.
- (7) Zhu, C.; Denis, S.; Nicolas, J. A Simple Route to Aqueous Suspensions of Degradable Copolymer Nanoparticles Based on Radical Ring-Opening Polymerization-Induced Self-Assembly (rRO-PISA). Chem. Mater. 2022, 34 (4), 1875–1888.
- (8) Varlas, S.; Neal, T. J.; Armes, S. P. Polymerization-induced self-assembly and disassembly during the synthesis of thermoresponsive ABC triblock copolymer nano-objects in aqueous solution. *Chem. Sci.* **2022**, *13* (24), 7295–7303.
- (9) Blackman, L. D.; Doncom, K. E. B.; Gibson, M. I.; O'Reilly, R. K. Comparison of photo- and thermally initiated polymerization-induced self-assembly: a lack of end group fidelity drives the formation of higher order morphologies. *Polym. Chem.* **2017**, *8* (18), 2860–2871.
- (10) Shahrokhinia, A.; Biswas, P.; Reuther, J. F. Orthogonal synthesis and modification of polymer materials. *J. Polym. Sci.* **2021**, 59 (16), 1748–1786.
- (11) Stache, E. E.; Kottisch, V.; Fors, B. P. Photocontrolled Radical Polymerization from Hydridic C-H Bonds. *J. Am. Chem. Soc.* **2020**, 142 (10), 4581–4585.
- (12) Chen, M.; Zhong, M.; Johnson, J. A. Light-Controlled Radical Polymerization: Mechanisms, Methods, and Applications. *Chem. Rev.* **2016**, *116* (17), 10167–10211.
- (13) Aydogan, C.; Yilmaz, G.; Shegiwal, A.; Haddleton, D. M.; Yagci, Y. Photoinduced Controlled/Living Polymerizations. *Angew. Chem., Int. Ed.* **2022**, *61* (23), No. e202117377.
- (14) Pan, X.; Tasdelen, M. A.; Laun, J.; Junkers, T.; Yagci, Y.; Matyjaszewski, K. Photomediated controlled radical polymerization. *Prog. Polym. Sci.* **2016**, *62*, 73–125.
- (15) Li, M.; Wang, S.; Li, F.; Zhou, L.; Lei, L. Iodine-mediated photo-controlled atom transfer radical polymerization (photo-ATRP) and block polymerization combined with ring-opening polymerization (ROP) via a superbase. *Polym. Chem.* **2020**, *11* (41), 6591–6598.
- (16) Xu, Q.; Tian, C.; Zhang, L.; Cheng, Z.; Zhu, X. Photo-Controlled Polymerization-Induced Self-Assembly (Photo-PISA): A Novel Strategy Using In Situ Bromine-Iodine Transformation Living

- Radical Polymerization. Macromol. Rapid Commun. 2019, 40 (2), 1800327.
- (17) Yeow, J.; Boyer, C. Photoinitiated Polymerization-Induced Self-Assembly (Photo-PISA): New Insights and Opportunities. *Advanced Science* **2017**, *4* (7), 1700137.
- (18) Ishizu, K.; Kakinuma, H. Synthesis of nanocylinders consisting of graft block copolymers by the photo-induced ATRP technique. *J. Polym. Sci., Part A: Polym. Chem.* **2005**, *43* (1), 63–70.
- (19) Anastasaki, A.; Nikolaou, V.; McCaul, N. W.; Simula, A.; Godfrey, J.; Waldron, C.; Wilson, P.; Kempe, K.; Haddleton, D. M. Photoinduced Synthesis of α,ω -Telechelic Sequence-Controlled Multiblock Copolymers. *Macromolecules* **2015**, 48 (5), 1404–1411.
- (20) Barbon, S. M.; Truong, N. P.; Elliott, A. G.; Cooper, M. A.; Davis, T. P.; Whittaker, M. R.; Hawker, C. J.; Anastasaki, A. Elucidating the effect of sequence and degree of polymerization on antimicrobial properties for block copolymers. *Polym. Chem.* **2020**, *11* (1), 84–90.
- (21) Shahrokhinia, A.; Scanga, R. A.; Biswas, P.; Reuther, J. F. PhotoATRP-Induced Self-Assembly (PhotoATR-PISA) Enables Simplified Synthesis of Responsive Polymer Nanoparticles in One-Pot. *Macromolecules* **2021**, *54* (3), 1441–1451.
- (22) Shahrokhinia, A.; Rijal, S.; Sonmez Baghirzade, B.; Scanga, R. A.; Biswas, P.; Tafazoli, S.; Apul, O. G.; Reuther, J. F. Chain Extensions in PhotoATRP-Induced Self-Assembly (PhotoATR-PISA): A Route to Ultrahigh Solids Concentrations and Click Nanoparticle Networks as Adsorbents for Water Treatment. *Macromolecules* **2022**, *55* (9), 3699–3710.
- (23) Ahn, S.-k.; Kasi, R. M.; Kim, S.-C.; Sharma, N.; Zhou, Y. Stimuli-responsive polymer gels. *Soft Matter* **2008**, *4* (6), 1151–1157. (24) Wei, M.; Gao, Y.; Li, X.; Serpe, M. J. Stimuli-responsive
- polymers and their applications. *Polym. Chem.* **2017**, 8 (1), 127–143. (25) Guragain, S.; Bastakoti, B. P.; Malgras, V.; Nakashima, K.;
- Yamauchi, Y. Multi-Stimuli-Responsive Polymeric Materials. *Chem.* Eur. J. **2015**, 21 (38), 13164—13174.
- (26) Bratek-Skicki, A. Towards a new class of stimuli-responsive polymer-based materials Recent advances and challenges. *Appl. Surf. Sci. Adv.* **2021**, *4*, 100068.
- (27) Hajebi, S.; Rabiee, N.; Bagherzadeh, M.; Ahmadi, S.; Rabiee, M.; Roghani-Mamaqani, H.; Tahriri, M.; Tayebi, L.; Hamblin, M. R. Stimulus-responsive polymeric nanogels as smart drug delivery systems. *Acta Biomater.* **2019**, *92*, 1–18.
- (28) Goponenko, A. V.; Dzenis, Y. A. Role of mechanical factors in applications of stimuli-responsive polymer gels Status and prospects. *Polymer* **2016**, *101*, 415–449.
- (29) Azcune, I.; Odriozola, I. Aromatic disulfide crosslinks in polymer systems: Self-healing, reprocessability, recyclability and more. *Eur. Polym. J.* **2016**, 84, 147–160.
- (30) Fortman, D. J.; Snyder, R. L.; Sheppard, D. T.; Dichtel, W. R. Rapidly Reprocessable Cross-Linked Polyhydroxyurethanes Based on Disulfide Exchange. *ACS Macro Lett.* **2018**, *7* (10), 1226–1231.
- (31) Bin Rusayyis, M.; Torkelson, J. M. Recyclable Polymethacrylate Networks Containing Dynamic Dialkylamino Disulfide Linkages and Exhibiting Full Property Recovery. *Macromolecules* **2020**, *53* (19), 8367–8373.
- (32) Patel, H. A.; Yavuz, M. S.; Yavuz, C. T. Exceptional organic solvent uptake by disulfide-linked polymeric networks. *RSC Adv.* **2014**, *4* (46), 24320–24323.
- (33) Canadell, J.; Goossens, H.; Klumperman, B. Self-Healing Materials Based on Disulfide Links. *Macromolecules* **2011**, 44 (8), 2536–2541.
- (34) Lei, Z. Q.; Xiang, H. P.; Yuan, Y. J.; Rong, M. Z.; Zhang, M. Q. Room-Temperature Self-Healable and Remoldable Cross-linked Polymer Based on the Dynamic Exchange of Disulfide Bonds. *Chem. Mater.* **2014**, *26* (6), 2038–2046.
- (35) Xu, Y.; Chen, D. A Novel Self-Healing Polyurethane Based on Disulfide Bonds. *Macromol. Chem. Phys.* **2016**, 217 (10), 1191–1196. (36) Altinbasak, I.; Arslan, M.; Sanyal, R.; Sanyal, A. Pyridyl disulfide-based thiol-disulfide exchange reaction: shaping the design

- of redox-responsive polymeric materials. *Polym. Chem.* **2020**, *11* (48), 7603–7624.
- (37) Shi, Z.; Wu, J.; Song, Q.; Göstl, R.; Herrmann, A. Toward Drug Release Using Polymer Mechanochemical Disulfide Scission. *J. Am. Chem. Soc.* **2020**, *142* (34), 14725–14732.
- (38) An, S. Y.; Noh, S. M.; Nam, J. H.; Oh, J. K. Dual Sulfide-Disulfide Crosslinked Networks with Rapid and Room Temperature Self-Healability. *Macromol. Rapid Commun.* **2015**, 36 (13), 1255–1260.
- (39) Wang, L.; Cao, Q.; Wang, X.; Wu, D. Visible light triggered controlled formation of rapidly self-healing hydrogels based on thiol-disulfide exchange. *Soft Matter* **2022**, *18* (15), 3004–3012.
- (40) Kong, L.; Xiong, Y.; Sun, L.; Tian, S.; Xu, X.; Zhao, C.; Luo, R.; Yang, X.; Shih, K.; Liu, H. Sorption performance and mechanism of a sludge-derived char as porous carbon-based hybrid adsorbent for benzene derivatives in aqueous solution. *J. Hazard. Mater.* **2014**, 274, 205–211.
- (41) Chen, D.; Chen, C.; Shen, W.; Quan, H.; Chen, S.; Xie, S.; Luo, X.; Guo, L. MOF-derived magnetic porous carbon-based sorbent: Synthesis, characterization, and adsorption behavior of organic micropollutants. *Adv. Powder Technol.* **2017**, 28 (7), 1769–1779.
- (42) Chakraborty, R.; K, V.; Pradhan, M.; Nayak, A. K. Recent advancement of biomass-derived porous carbon based materials for energy and environmental remediation applications. *J. Mater. Chem. A* **2022**, *10* (13), 6965–7005.
- (43) Chen, Y.; Fan, C.; Li, X.; Ren, J.; Zhang, G.; Xie, H.; Liu, B.; Zhou, G. Preparation of carbon black-based porous carbon adsorbents and study of toluene adsorption properties. *J. Chem. Technol. Biotechnol.* **2023**, 98 (1), 117–128.
- (44) Gopinath, K. P.; Vo, D.-V. N.; Gnana Prakash, D.; Adithya Joseph, A.; Viswanathan, S.; Arun, J. Environmental applications of carbon-based materials: a review. *Environ. Chem. Lett.* **2021**, *19* (1), 557–582.
- (45) Bhatnagar, A.; Hogland, W.; Marques, M.; Sillanpää, M. An overview of the modification methods of activated carbon for its water treatment applications. *Chem. Eng. J.* **2013**, 219, 499–511.
- (46) Kumarasamy, E.; Manning, I. M.; Collins, L. B.; Coronell, O.; Leibfarth, F. A. Ionic Fluorogels for Remediation of Per- and Polyfluorinated Alkyl Substances from Water. ACS Cent. Sci. 2020, 6 (4), 487–492.
- (47) He, J.; Gomeniuc, A.; Olshansky, Y.; Hatton, J.; Abrell, L.; Field, J. A.; Chorover, J.; Sierra-Alvarez, R. Enhanced removal of perand polyfluoroalkyl substances by crosslinked polyaniline polymers. *Chem. Eng. J.* **2022**, 446, 137246.
- (48) Tan, X.; Dewapriya, P.; Prasad, P.; Chang, Y.; Huang, X.; Wang, Y.; Gong, X.; Hopkins, T. E.; Fu, C.; Thomas, K. V.; Peng, H.; Whittaker, A. K.; Zhang, C. Efficient Removal of Perfluorinated Chemicals from Contaminated Water Sources Using Magnetic Fluorinated Polymer Sorbents. *Angew. Chem., Int. Ed.* **2022**, *61* (49), No. e202213071.
- (49) Harris, J. T.; de la Garza, G. D.; Devlin, A. M.; McNeil, A. J. Rapid Removal of Poly- and Perfluoroalkyl Substances with Quaternized Wood Pulp. ACS ES&T Water 2022, 2 (2), 349–356.
- (50) Ateia, M.; Arifuzzaman, M.; Pellizzeri, S.; Attia, M. F.; Tharayil, N.; Anker, J. N.; Karanfil, T. Cationic polymer for selective removal of GenX and short-chain PFAS from surface waters and wastewaters at ng/L levels. *Water Res.* **2019**, *163*, 114874.
- (51) Klemes, M. J.; Skala, L. P.; Ateia, M.; Trang, B.; Helbling, D. E.; Dichtel, W. R. Polymerized Molecular Receptors as Adsorbents to Remove Micropollutants from Water. *Acc. Chem. Res.* **2020**, *53* (10), 2314–2324.
- (52) Ramos, P.; Singh Kalra, S.; Johnson, N. W.; Khor, C. M.; Borthakur, A.; Cranmer, B.; Dooley, G.; Mohanty, S. K.; Jassby, D.; Blotevogel, J.; Mahendra, S. Enhanced removal of per- and polyfluoroalkyl substances in complex matrices by polyDADMAC-coated regenerable granular activated carbon. *Environ. Pollut.* 2022, 294, 118603.
- (53) Gagliano, E.; Sgroi, M.; Falciglia, P. P.; Vagliasindi, F. G. A.; Roccaro, P. Removal of poly- and perfluoroalkyl substances (PFAS)

- from water by adsorption: Role of PFAS chain length, effect of organic matter and challenges in adsorbent regeneration. *Water Res.* **2020**, *171*, 115381.
- (54) Beattie, D. L.; Mykhaylyk, O. O.; Armes, S. P. Enthalpic incompatibility between two steric stabilizer blocks provides control over the vesicle size distribution during polymerization-induced self-assembly in aqueous media. *Chem. Sci.* **2020**, *11* (39), 10821–10834.
- (55) Dhiraj, H. S.; Ishizuka, F.; Elshaer, A.; Zetterlund, P. B.; Aldabbagh, F. RAFT dispersion polymerization induced self-assembly (PISA) of boronic acid-substituted acrylamides. *Polym. Chem.* **2022**, *13* (25), 3750–3755.
- (56) Qu, Y.; Wang, S.; Khan, H.; Gao, C.; Zhou, H.; Zhang, W. One-pot preparation of BAB triblock copolymer nano-objects through bifunctional macromolecular RAFT agent mediated dispersion polymerization. *Polym. Chem.* **2016**, *7* (10), 1953–1962.
- (57) Biais, P.; Beaunier, P.; Stoffelbach, F.; Rieger, J. Loop-stabilized BAB triblock copolymer morphologies by PISA in water. *Polym. Chem.* **2018**, 9 (35), 4483–4491.
- (58) Biais, P.; Colombani, O.; Bouteiller, L.; Stoffelbach, F.; Rieger, J. Unravelling the formation of BAB block copolymer assemblies during PISA in water. *Polym. Chem.* **2020**, *11* (28), 4568–4578.
- (59) Nicolai, T.; Colombani, O.; Chassenieux, C. Dynamic polymeric micelles versus frozen nanoparticles formed by block copolymers. *Soft Matter* **2010**, *6* (14), 3111–3118.
- (60) Khor, S. Y.; Quinn, J. F.; Whittaker, M. R.; Truong, N. P.; Davis, T. P. Controlling Nanomaterial Size and Shape for Biomedical Applications via Polymerization-Induced Self-Assembly. *Macromol. Rapid Commun.* **2019**, 40 (2), 1800438.
- (61) Apul, O. G.; Wang, Q.; Zhou, Y.; Karanfil, T. Adsorption of aromatic organic contaminants by graphene nanosheets: Comparison with carbon nanotubes and activated carbon. *Water Res.* **2013**, *47* (4), 1648–1654.
- (62) Michal, B. T.; Jaye, C. A.; Spencer, E. J.; Rowan, S. J. Inherently Photohealable and Thermal Shape-Memory Polydisulfide Networks. *ACS Macro Lett.* **2013**, 2 (8), 694–699.
- (63) Fairbanks, B. D.; Singh, S. P.; Bowman, C. N.; Anseth, K. S. Photodegradable, Photoadaptable Hydrogels via Radical-Mediated Disulfide Fragmentation Reaction. *Macromolecules* **2011**, 44 (8), 2444–2450.
- (64) da Silva, J. F.; Morais, A. T. d. B.; Santos, W. G.; M Ahrné, L.; Cardoso, D. R. UV-C light promotes the reductive cleavage of disulfide bonds in β -Lactoglobulin and improves in vitro gastric digestion. *Food Res. Int.* **2023**, *168*, 112729.
- (65) Zhao, D.; Du, Z.; Liu, S.; Wu, Y.; Guan, T.; Sun, Q.; Sun, N.; Ren, B. UV Light Curable Self-Healing Superamphiphobic Coatings by Photopromoted Disulfide Exchange Reaction. ACS Appl. Polym. Mater. 2019, 1 (11), 2951–2960.
- (66) Santadkha, T.; Skolpap, W.; Thitapakorn, V. Diffusion Modeling and In Vitro Release Kinetics Studies of Curcumin-Loaded Superparamagnetic Nanomicelles in Cancer Drug Delivery System. *J. Pharm. Sci.* **2022**, *111* (6), 1690–1699.
- (67) Lisik, A.; Musiał, W. Conductomeric Evaluation of the Release Kinetics of Active Substances from Pharmaceutical Preparations Containing Iron Ions. *Materials (Basel)* **2019**, *12* (5), 730.
- (68) Costa, P.; Sousa Lobo, J. M. Modeling and comparison of dissolution profiles. *Eur. J. Pharm. Sci.* **2001**, *13* (2), 123–133.
- (69) Peppas, N. A.; Narasimhan, B. Mathematical models in drug delivery: How modeling has shaped the way we design new drug delivery systems. *J. Controlled Release* **2014**, *190*, 75–81.